

## Research Article

# Nanowrinkled Carbon Aerogels Embedded with FeN<sub>x</sub> Sites as Effective Oxygen Electrodes for Rechargeable Zinc-Air Battery

Ting He <sup>1,2</sup>, Bingzhang Lu,<sup>2</sup> Yang Chen,<sup>1</sup> Yong Wang,<sup>1</sup> Yaqiang Zhang,<sup>3</sup> John L. Davenport <sup>4</sup>, Alan P. Chen,<sup>4</sup> Chih-Wen Pao <sup>5</sup>, Min Liu,<sup>6</sup> Zhifang Sun,<sup>1</sup> Alexander Stram <sup>4</sup>, Alexander Mordaunt <sup>4</sup>, Jairo Velasco Jr. <sup>4</sup>, Yuan Ping,<sup>2</sup> Yi Zhang <sup>1,7</sup>, and Shaowei Chen <sup>2</sup>

<sup>1</sup>State Key Laboratory for Powder Metallurgy, College of Chemistry and Chemical Engineering, Central South University, Changsha 410083, China

<sup>2</sup>Department of Chemistry and Biochemistry, University of California, 1156 High Street, Santa Cruz, California 95064, USA

<sup>3</sup>Department of Chemical and Materials Engineering, University of Alberta, Edmonton, Alberta, Canada T6G 1H9

<sup>4</sup>Department of Physics, University of California, 1156 High Street, Santa Cruz, California 95064, USA

<sup>5</sup>X-Ray Absorption Group, National Synchrotron Radiation Research Center, Hsinchu 30076, Taiwan

<sup>6</sup>Institute of Super-Microstructure and Ultrafast Process in Advanced Materials, School of Physics and Electronics, Central South University, Changsha 410083, China

<sup>7</sup>Key Laboratory of Materials Processing and Mold (Zhengzhou University), Ministry of Education, Zhengzhou 450002, China

Correspondence should be addressed to Yi Zhang; [yzhangcsu@csu.edu.cn](mailto:yzhangcsu@csu.edu.cn) and Shaowei Chen; [shaowei@ucsc.edu](mailto:shaowei@ucsc.edu)

Received 26 September 2019; Accepted 12 November 2019; Published 20 December 2019

Copyright © 2019 Ting He et al. Exclusive Licensee Science and Technology Review Publishing House. Distributed under a Creative Commons Attribution License (CC BY 4.0).

Rational design of single-metal atom sites in carbon substrates by a flexible strategy is highly desired for the preparation of high-performance catalysts for metal-air batteries. In this study, biomass hydrogel reactors are utilized as structural templates to prepare carbon aerogels embedded with single iron atoms by controlled pyrolysis. The tortuous and interlaced hydrogel chains lead to the formation of abundant nanowrinkles in the porous carbon aerogels, and single iron atoms are dispersed and stabilized within the defective carbon skeletons. X-ray absorption spectroscopy measurements indicate that the iron centers are mostly involved in the coordination structure of FeN<sub>4</sub>, with a minor fraction (ca. 1/5) in the form of FeN<sub>3</sub>C. First-principles calculations show that the FeN<sub>x</sub> sites in the Stone-Wales configurations induced by the nanowrinkles of the hierarchically porous carbon aerogels show a much lower free energy than the normal counterparts. The resulting iron and nitrogen-codoped carbon aerogels exhibit excellent and reversible oxygen electrocatalytic activity, and can be used as bifunctional cathode catalysts in rechargeable Zn-air batteries, with a performance even better than that based on commercial Pt/C and RuO<sub>2</sub> catalysts. Results from this study highlight the significance of structural distortions of the metal sites in carbon matrices in the design and engineering of highly active single-atom catalysts.

## 1. Introduction

Climate change and environmental pollution have motivated the development of sustainable, clean energy technologies, of which rechargeable metal-air batteries have drawn tremendous attention owing to their high energy density and minimal impacts on the environment [1–4]. The overall efficiency of the charge-discharge process of metal-air batteries is determined by two major reactions, oxygen reduction reaction

(ORR) and oxygen evolution reaction (OER). Although platinum group metal (PGM) materials, such as Pt/C, RuO<sub>2</sub>, and Ir/C, possess excellent catalytic activity for either ORR or OER, none of these noble metal catalysts displays a satisfactory performance for both [5], and their scarcity and high costs greatly hinder their practical applications [6, 7]. Therefore, development of bifunctional catalysts with a low cost and high activity is of both fundamental and technological significance, but remains a great challenge.

Recent studies have demonstrated that PGM-free nanocomposites based on carbon materials, such as heteroatom- (including nonmetal and metal atoms) doped porous carbon, are promising bifunctional oxygen catalysts [8–10]. In fact, transition metal-doped carbon catalysts have been widely investigated due to the unique chemical properties caused by their adjustable 3D electronic orbitals. In particular, transition metal-based single-atom catalysts display overwhelming superiority as compared to their nanoparticle and nanocluster counterparts [11–15]. For instance, single-site dispersion of  $\text{FeN}_x$  species in a two-dimensional nitrogen-doped porous carbon layer has been found to exhibit a remarkable catalytic activity towards both ORR and OER in alkaline media [1], where a range of catalytic active sites has been proposed, such as  $\text{CoN}_2\text{C}_2$ ,  $\text{FeN}_3\text{C}$ ,  $\text{FeN}_4$ , and  $\text{FeN}_4\text{O}$  [16–18]. However, the effects of structural distortion induced by the single-metal sites on the catalytic activity have long been ignored, although such structural defects are common in pyrolytic carbon.

Herein, biomass hydrogels (i.e., chitosan, gelatin, and agar), which have long been known for their diverse applications and economic advantages [19, 20], were prepared and used as unique precursors, templates, and reactors to produce three-dimensional, nanowrinkled carbon aerogels embedded with  $\text{FeN}_x$  single sites [21–23]. Due to the abundant functional groups on the hydrogel chains, defective single-metal sites were dispersed and stabilized within the nanowrinkled, porous carbon aerogels. First-principles calculations showed that the  $\text{FeN}_x$  sites in the Stone-Wales configurations induced by the carbon nanowrinkles displayed a much lower free energy for oxygen electrocatalysis than the normal counterparts. Electrochemical measurements exhibited apparent and reversible oxygen electrocatalytic performance towards both ORR and OER. When the nanowrinkled carbon aerogels were used as the air-cathode of a zinc-air battery, the battery displayed a higher open-circuit voltage and higher energy density, as well as better cycling stability than that with commercial Pt/C- $\text{RuO}_2$  catalysts.

## 2. Results and Discussion

**2.1. Synthesis and Characterization.** In this study, flexible biomass hydrogels were synthesized in a facile process and employed as 3D templates to prepare carbon aerogels embedded with single-metal atoms (Figures 1(a) and S1). In order to achieve atomic dispersion, the hydrogel networks were modified by two strategies to minimize metal aggregation. The first is “headstream fixation,” which means immobilization of metal atoms into the hydrogel reactor by complexation agents (e.g., phenanthroline (PM)); and the other, “roadblocks,” is based on rigid templates, such as  $\text{SiO}_2$  nanoparticles and Zn atoms. Experimentally, a variety of hydrogel/hydrosol networks, i.e.,  $\text{CS}_{\text{Si-Zn}}/\text{FePM}$ ,  $\text{CS}_{\text{Si}}/\text{FePM}$ ,  $\text{CS}_{\text{Si}}/\text{Fe}$ , and  $\text{CS}_{\text{Si}}$ , were prepared by using chitosan (CS) as the structural scaffold, along with a select combination of other precursors, such as  $\text{SiO}_2$  nanoparticles (Si), FePM, and Zn salt (details in Materials and Methods). The morphological details were first investigated by scanning

electron microscopy (SEM) measurements. From Figure S2, freeze-dried  $\text{CS}_{\text{Si}}/\text{FePM}$ ,  $\text{CS}_{\text{Si}}/\text{Fe}$ , and  $\text{CS}_{\text{Si}}$  hydrosols can be seen to consist of uneven microcavities. However, as shown in Figure 1(b), the microcavities of the  $\text{CS}_{\text{Si-Zn}}/\text{FePM}$  hydrogel shows a more uniform size of ca.  $50\ \mu\text{m}$ , forming a 3D, continuous framework composed of intertwining CS-Zn chains. This suggests that Zn ions can induce the hydrogelation of CS hydrosol to form much more uniform 3D intertwining networks, which further facilitates the generation of nanowrinkles [24]. Circular dichroism (CD) and UV-vis absorption measurements were then carried out to monitor the structural evolution from  $\text{CS}_{\text{Si}}$  sol to  $\text{CS}_{\text{Si-Zn}}/\text{FePM}$  hydrogel. As depicted in Figure S3a, the incorporation of both FePM and  $\text{Zn}^{2+}$  ions into chitosan led to marked conformational changes of the CS chains. In UV-vis absorption measurements (Figure S3b), two new peaks can be seen to emerge at ca. 226 nm and 268 nm, due to the strong complexation interaction between Fe and PM [25].

The freeze-dried  $\text{CS}_{\text{Si-Zn}}/\text{FePM}$  hydrogel was then used as a 3D reactor to synthesize metal-doped carbon aerogels by controlled pyrolysis, which was then subject to HF etching to remove the  $\text{SiO}_2$  templates (Figure 1(a)), producing  $\text{NCA}_{\text{C-Zn}}/\text{Fe}$  (Figure 1(c) inset). Control samples of  $\text{NCA}_{\text{C}}/\text{Fe}$ ,  $\text{CA}_{\text{C}}/\text{Fe}$ , and  $\text{CA}_{\text{C}}$  were prepared in a similar fashion (details in Materials and Methods). From the transmission electron microscopy (TEM) images in Figure S4, one can see that the  $\text{NCA}_{\text{C-Zn}}/\text{Fe}$  sample displays a highly porous, nanowrinkled structure with rich mesopores of ca. 10 nm in diameter. In both bright-field (Figure 1(c)) and dark-field (Figure 1(d)) scanning transmission electron microscopy (STEM) images, one can clearly see the formation of single-metal atoms (red circles) embedded into the porous carbon matrix. The corresponding elemental maps clearly show that the C, N, and Fe elements are homogeneously distributed across the aerogel (Figure 1(e)). These results indicate successful construction of N-doped carbon aerogels embedded with isolated Fe atoms by using biomass hydrogels as the reactors.

In order to examine the mechanical and electrical properties of the obtained porous carbon, Fast Force Mapping (FFM) measurements were then carried out. The data presented in Figures 1(f)–1(g) and S5 exhibit a ca. 10 nm variation in the mechanical and electrical properties of the porous carbon, confirming the formation of nanowrinkled carbon. Domains dictated by round features in topography (Figure S5a) are outlined by prominent changes in max force (Figure S5b) and an increase in the adhesion force (Figure 1(f)). Notably, the adhesion force, which represents the bulk modulus or stiffness of the sample, indicates that these round regions are stiffer in the center and softer around the edges. Typically,  $\text{sp}^2$ -hybridized carbon exhibits hydrophobic characteristics, whereas defective carbons are more hydrophilic [26, 27]. With an AFM tip that consists of a hydrophilic silicon oxide layer, a high adhesion force corresponds to a hydrophilic domain. This implies that the metal centers are most likely situated within the high adhesion force areas. Interestingly, from Figures 1(f) to 1(g), one can see that the soft nodes correspond to high electrical conductance. Taken together, these results suggest that the metal sites are mostly located in

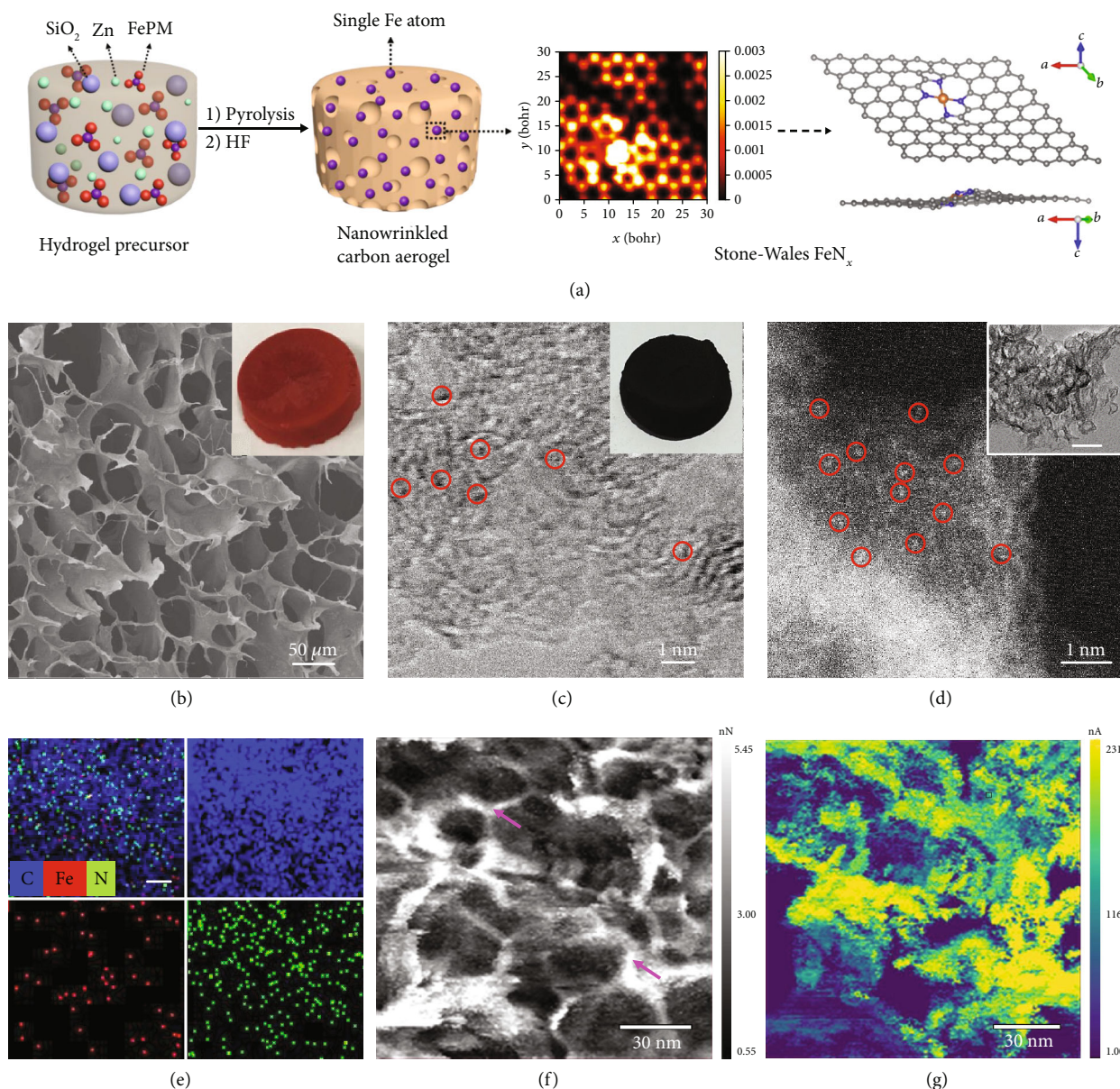


FIGURE 1: Synthesis and morphological characterization of the  $\text{NCA}_{\text{C-Zn}}/\text{Fe}$  carbon aerogel. (a) Schematic representation of the synthesis of the  $\text{NCA}_{\text{C-Zn}}/\text{Fe}$  carbon aerogel. (b) SEM image of the freeze-dried  $\text{CS}_{\text{Si-Zn}}/\text{FePM}$  hydrogel. Inset is a digital photo of the sample. (c) Bright-field STEM image of the  $\text{NCA}_{\text{C-Zn}}/\text{Fe}$  aerogel. Red circles indicate single Fe atoms. Inset is a digital photo of the sample. (d) Dark-field STEM image of the  $\text{NCA}_{\text{C-Zn}}/\text{Fe}$  aerogel. Red circles indicate single Fe atoms. Inset is a TEM image of the  $\text{NCA}_{\text{C-Zn}}/\text{Fe}$  aerogel, and the scale bar is 30 nm. (e) Elemental maps of  $\text{NCA}_{\text{C-Zn}}/\text{Fe}$  aerogels. The scale bar is 10 nm. AFM images of  $\text{NCA}_{\text{C-Zn}}/\text{Fe}$  aerogels: (f) adhesion force image and (g) current flow image.

the high adhesion and high conductivity areas of the porous carbon aerogel [28, 29]. Both features are conducive to oxygen electrocatalysis.

The porosity of the obtained samples was then quantitatively evaluated by  $\text{N}_2$  adsorption-desorption measurements. The carbon aerogels obtained above all show a Type IV isotherm (Figures 2(a) and S6a), which suggests the formation of a complex porous network containing a myriad of mesopores with an average size of ca. 10 nm, in line with the diameter of the  $\text{SiO}_2$  nanoparticle [30]. From the isotherms, the specific surface area of  $\text{NCA}_{\text{C-Zn}}/\text{Fe}$  was estimated to be

$609 \text{ m}^2 \text{ g}^{-1}$ , with a microporous surface area of  $111 \text{ m}^2 \text{ g}^{-1}$ , which is the highest among the series, a condition favorable for the formation of abundant active sites (Figure S6b and Table S1). The corresponding X-ray powder diffraction (XRD) patterns are shown in Figure S7, where only one broad peak at ca.  $25^\circ$  can be observed, due to the (002) diffraction of graphitic carbon [31]. This carbon diffraction became gradually sharpened from  $\text{CS}_{\text{C}}$  to  $\text{NCA}_{\text{C-Zn}}/\text{Fe}$ , indicating an increasing degree of graphitization. Importantly, the fact that no other diffraction features were observed suggests the absence of metal (oxide) nanoparticles.

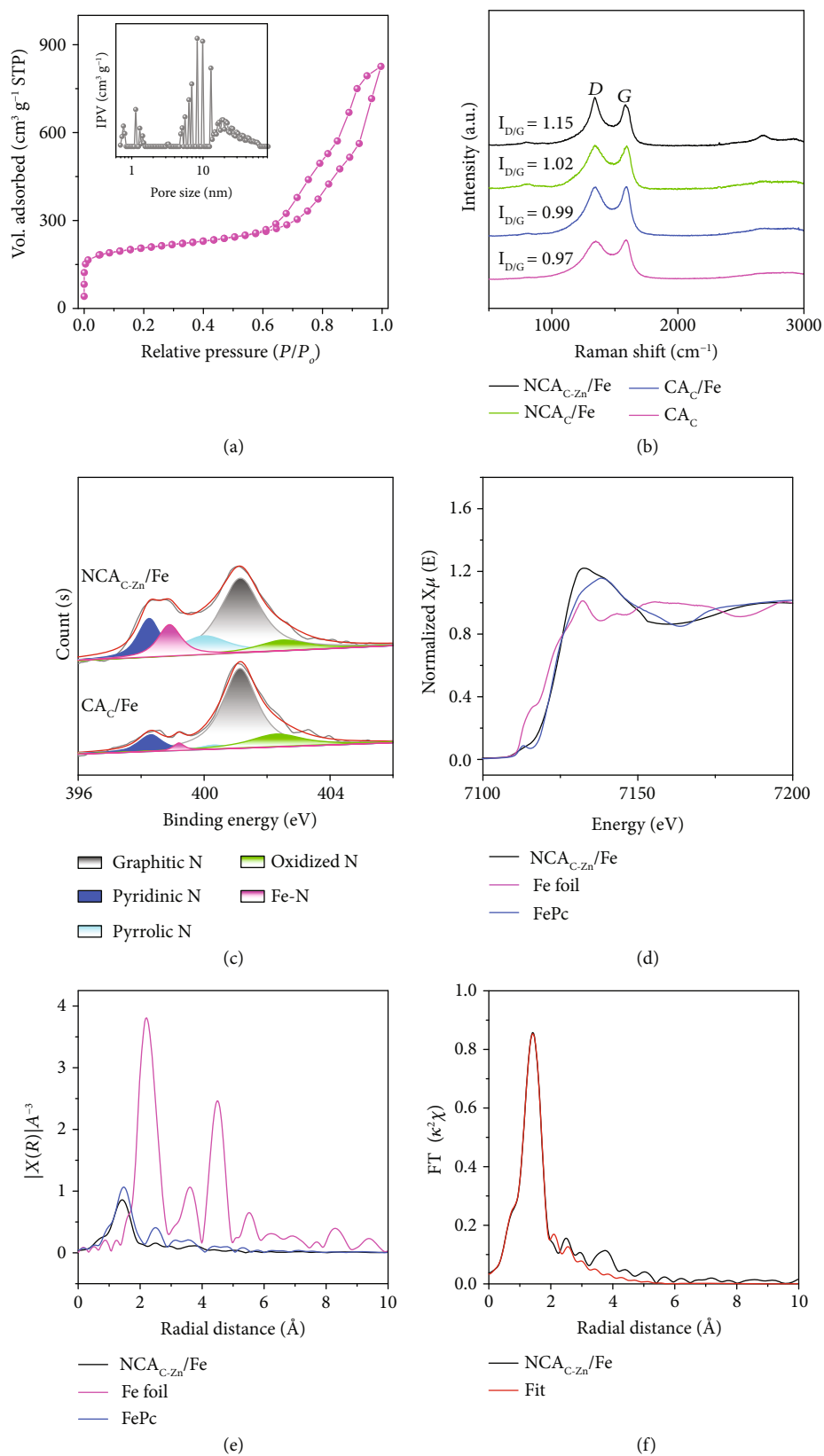


FIGURE 2: Structural characterization of the  $NCA_{C-Zn}/Fe$  carbon aerogel. (a)  $N_2$  adsorption-desorption isotherm of  $NCA_{C-Zn}/Fe$ . Inset is the corresponding pore size distribution. (b) Raman spectra of  $CA_C$ ,  $CA_C/Fe$ ,  $NCA_C/Fe$ , and  $NCA_{C-Zn}/Fe$ . (c) XPS spectra of the N 1s electrons in  $CA_C/Fe$  and  $NCA_{C-Zn}/Fe$ . (d) K-edge XANES of  $NCA_{C-Zn}/Fe$ , FePc, and Fe foil. (e) K-edge EXAFS of  $NCA_{C-Zn}/Fe$ , FePc, and Fe foil. (f) The corresponding EXAFS fitting curves for the  $NCA_{C-Zn}/Fe$  sample.

In Raman measurements, the  $I_D/I_G$  ratio of  $\text{NCA}_{\text{C-Zn}}/\text{Fe}$  was estimated to be ca. 1.15, much higher than those of the control samples (Figure 2(b)), signifying the generation of rich defects which may be conducive to the formation of metal active sites [31].

The elemental compositions of the obtained carbon samples were then quantitatively assessed by inductively coupled plasma atomic emission spectroscopy (ICP-OES) and energy-dispersive X-ray spectroscopy (EDS) measurements. Results from ICP-OES analysis showed that the Fe content in the carbon aerogel was about 0.22 wt% for  $\text{CA}_{\text{C}}/\text{Fe}$ , 0.61 wt% for  $\text{NCA}_{\text{C}}/\text{Fe}$ , and 0.72 wt% for  $\text{NCA}_{\text{C-Zn}}/\text{Fe}$ , in good accordance with the EDS results (Figure S8, Tables S2 and S3). The increased metal content suggests the important roles of PM (chelation) and  $\text{Zn}^{2+}$  ions (porogen and gel initiator) into fixing Fe centers in the carbon matrix. Further analysis was conducted with X-ray photoelectron spectroscopy (XPS) measurements. First of all, no Fe–O peak can be resolved in the high-resolution scan of the O 1s electrons (Figure S9a), suggesting that Fe atoms are most likely coordinated to other atomic sites such as N and C; and from the XPS spectra of the N 1s electrons of the series of samples (Figures 2(c), S9b, and S9c), one can see that the successive introduction of PM and  $\text{Zn}^{2+}$  into the precursors increased the N doping from 2.25 at% to 3.60 at% in the carbon matrix (Tables S4 and S5), and the pyridinic N fraction was the highest in the  $\text{NCA}_{\text{C}}/\text{Fe}$  (0.52 at%) and  $\text{NCA}_{\text{C-Zn}}/\text{Fe}$  (0.51 at%) samples. In addition, as compared to  $\text{CS}_{\text{C}}/\text{Fe}$ , the much stronger Fe–N peak (0.44 at% vs. 0.04 at%) in the  $\text{NCA}_{\text{C-Zn}}/\text{Fe}$  sample suggests the generation of more abundant  $\text{FeN}_x$  moieties in the carbon aerogels.

The structural configuration of the  $\text{FeN}_x$  functional moiety was then examined by X-ray absorption spectroscopy (XAS) measurements. From Figure 2(d), one can see that the Fe K-edge X-ray absorption near-edge spectrum (XANES) of  $\text{NCA}_{\text{C-Zn}}/\text{Fe}$  is very similar to that of FePc but markedly different from that of an Fe foil, suggesting a comparable oxidation state (+2) of the Fe centers in  $\text{NCA}_{\text{C-Zn}}/\text{Fe}$  and FePc. In the extended X-ray absorption fine structure (EXAFS) spectrum of the Fe foil, the Fe–Fe peak is well-defined at 2.21 Å (Figure 2(e)); however, this peak is absent in  $\text{NCA}_{\text{C-Zn}}/\text{Fe}$ , consistent with the atomic dispersion of Fe in the  $\text{NCA}_{\text{C-Zn}}/\text{Fe}$  sample (Figure 1). In fact, both the  $\text{NCA}_{\text{C-Zn}}/\text{Fe}$  and FePc samples display only a single major peak at 1.41 Å, which can be assigned to the Fe–N bond. Furthermore, the first shell of  $\text{NCA}_{\text{C-Zn}}/\text{Fe}$  is well fitted with 3.8 N and 0.2 C with the same bond length of 1.94 Å (Figures 2(f) and S10). Taken together, these results suggest that the Fe centers in  $\text{NCA}_{\text{C-Zn}}/\text{Fe}$  were mostly involved in the coordination structure of  $\text{FeN}_4$ , with a minor fraction (ca. 1/5) in the form of  $\text{FeN}_3\text{C}$ .

**2.2. Theoretical Investigation of the ORR Using the  $\text{NCA}_{\text{C-Zn}}/\text{Fe}$  Catalyst.** First-principles calculations were then carried out to shed light on the contributions of  $\text{FeN}_4$  and  $\text{FeN}_3\text{C}$  moieties to the electrocatalytic activity. It is likely that the interlaced 3D structure of the hydrogel networks and the tortuous CS chains can lead to the formation of abundant

wrinkles in the obtained porous carbon aerogels. Therefore, the electrocatalytic activities of the Stone-Wales- (SW-) defect  $\text{FeN}_4$  ( $\text{FeN}_4$  SW) and  $\text{FeN}_3\text{C}$  ( $\text{FeN}_3\text{C}$  SW) moieties, which can be formed by the nanowrinkles of carbon matrices, are examined by theoretical calculations. Figures 3(a)–3(b) and S11 show the side view and top view of the atomic models of the four kinds of Fe–N centers. From the atomic models, one can see that the normal  $\text{FeN}_4$  and normal  $\text{FeN}_3\text{C}$  moieties exhibit a planar structure in the carbon matrices, while  $\text{FeN}_4$  SW and  $\text{FeN}_3\text{C}$  SW show a distorted nonplanar structure. The simulated scanning tunneling microscopic (STM) images of the  $\text{FeN}_4$  and  $\text{FeN}_4$  SW moieties are presented in Figures 3(c)–3(d) and S12. As compared to normal  $\text{FeN}_4$ , the SW defects cause significant redistribution of electron densities of  $\text{FeN}_4$  and adjacent carbon atoms. Figure 3(e) displays the total density of states (DOS) of normal and SW Fe–N centers. According to Figure 3(f), for the  $\text{FeN}_4$  SW on a graphene sheet, the Fe atom makes the largest contributions to the DOS near the Fermi level (red peak), which is similar to that (black line) of normal  $\text{FeN}_4$ . Apparently, the marked state of  $\text{FeN}_4$  SW (highlighted by arrows in Figure 3(e)) is much closer to the Fermi level than that of normal  $\text{FeN}_4$ , indicating a higher probability of donating electrons and reducing oxygen.

To evaluate the ORR activity of these Fe–N metal centers, the reaction free energy is calculated at the applied potential of +0.9 V vs. RHE and plotted in Figure 3(g). One can see that the first two electron-transfer steps are exothermic and the last two endothermic, with the rate determining step (RDS) most likely the fourth electron-transfer step of water formation and desorption. In comparison with normal  $\text{FeN}_4$  and  $\text{FeN}_3$ , both  $\text{FeN}_4$  SW and  $\text{FeN}_3$  SW show much lower endothermic energies (0.179 eV and 0.228 eV), implying a lower reaction overpotential. These results suggest that the nanowrinkles can enhance the electrocatalytic activity of Fe–N centers on the carbon matrices by forming SW defects, as manifested below in electrochemical tests.

**2.3. Electrocatalytic Activity towards ORR.** The electrocatalytic activity of the nanowrinkled carbon aerogels obtained above was then investigated in 0.1 M KOH. First, electrical impedance spectroscopy (EIS) analysis was carried out to investigate the electron-transfer kinetics. For the  $\text{NCA}_{\text{C-Zn}}/\text{Fe}$  catalyst, the small diameter at high frequency and the steep tail at low frequency suggest excellent channels for both mass transfer and charge transfer. Such a low impedance is anticipated to facilitate ORR electrocatalysis (Figure S13). Figures 4(a) and 4(b) show the ORR polarization curves and  $\text{H}_2\text{O}_2$  yields of the carbon aerogels, in comparison to commercial Pt/C (20 wt%). As a metal-free catalyst, the  $\text{CA}_{\text{C}}$  sample shows a rather apparent electrocatalytic activity with an onset potential ( $E_{\text{onset}}$ ) of +0.94 V vs. RHE and a half-wave potential ( $E_{1/2}$ ) of +0.79 V, much more positive than those of other carbon catalysts reported in recent literature [15, 32, 33]. This suggests that biomass alone may be exploited as a carbon source to fabricate metal-free ORR electrocatalysts. Notably, doping of the FePM complex into the  $\text{CS}_{\text{Si}}$  leads to a marked enhancement of the catalytic performance with  $E_{\text{onset}} = +$

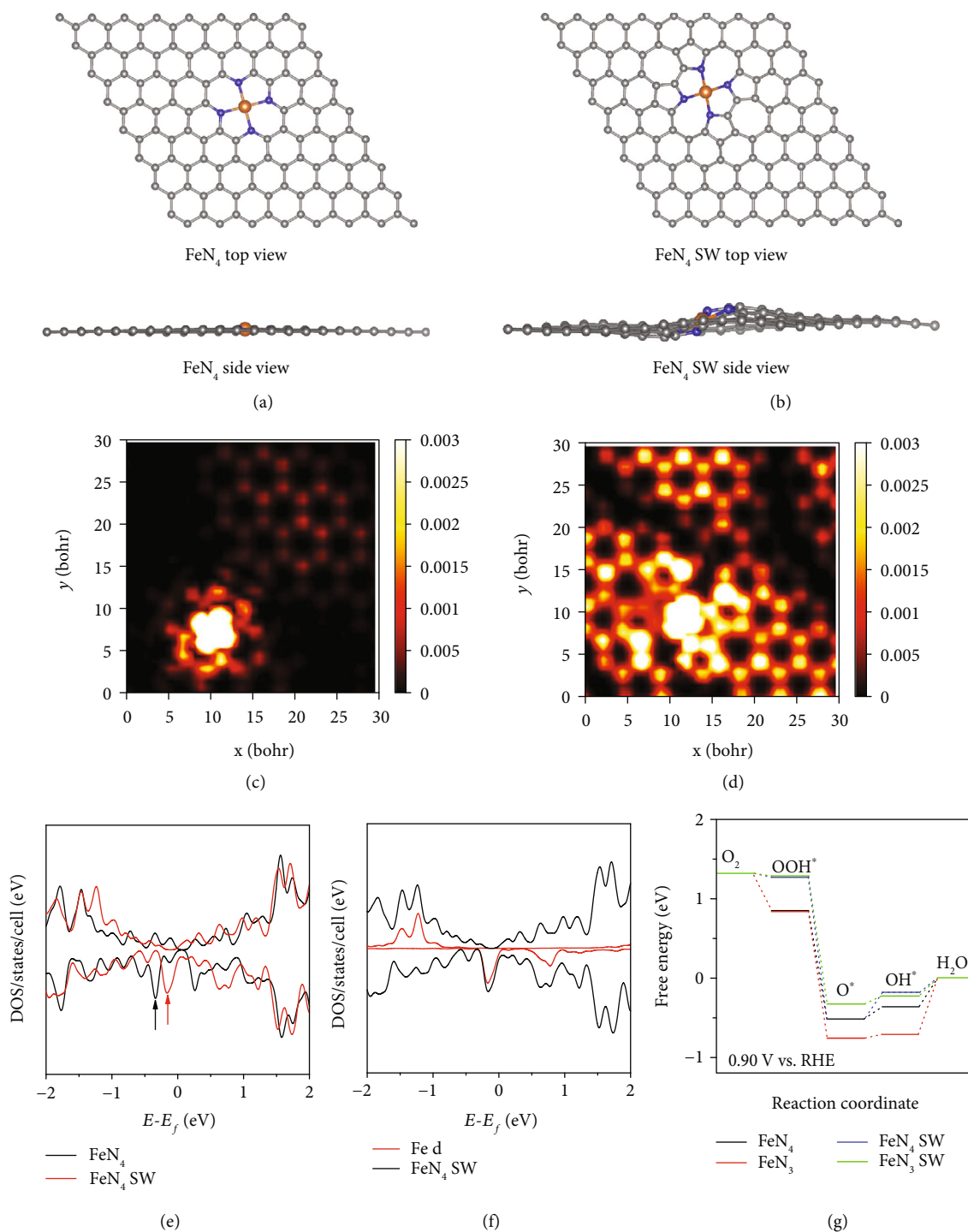


FIGURE 3: Atomic model and DOS of metal sites; Gibbs free energy diagrams of ORR. (a, c) Side/top view and simulated STM image (at a bias of  $-1.0$  V) of normal FeN<sub>4</sub> doped graphene sheets. (b, d) Side/top view and simulated STM image (at a bias of  $-1.0$  V) of Stone-Wales FeN<sub>4</sub>- (FeN<sub>4</sub> SW-) doped graphene sheets. (e) Density of state (DOS) of normal FeN<sub>4</sub> and FeN<sub>4</sub> SW-doped graphene sheets. (f) DOS of FeN<sub>4</sub> SW and Fe 3d. (g) Free energy diagrams of ORR processes on normal FeN<sub>4</sub>, normal FeN<sub>3</sub>, FeN<sub>4</sub> SW, and FeN<sub>3</sub> SW at the applied potential of  $+0.9$  V vs. RHE.

$1.10$  V and  $E_{1/2} = +0.90$  V (NCA<sub>C-Zn</sub>/Fe), which is even better than those of commercial Pt/C ( $+0.99$  V and  $+0.83$  V) [34]. Likewise, the NCA<sub>C-Zn</sub>/Fe single-atom catalyst shows the lowest average H<sub>2</sub>O<sub>2</sub> yield (1.45%) within the potential range of  $+0.2$  V to  $+0.9$  V, signifying a high-

efficiency  $4e^-$  reduction pathway (Figures S14–S16). From the Koutecky-Levich plots, the kinetic current density ( $J_k$ ) at  $+0.85$  V was estimated to be  $9.12$  mA cm<sup>-2</sup>, about 3.3 times that of Pt/C ( $2.80$  mA cm<sup>-2</sup>, Figure 4(c)). Both NCA<sub>C-Zn</sub>/Fe and Pt/C show a low Tafel slope (85 vs. 87 mV

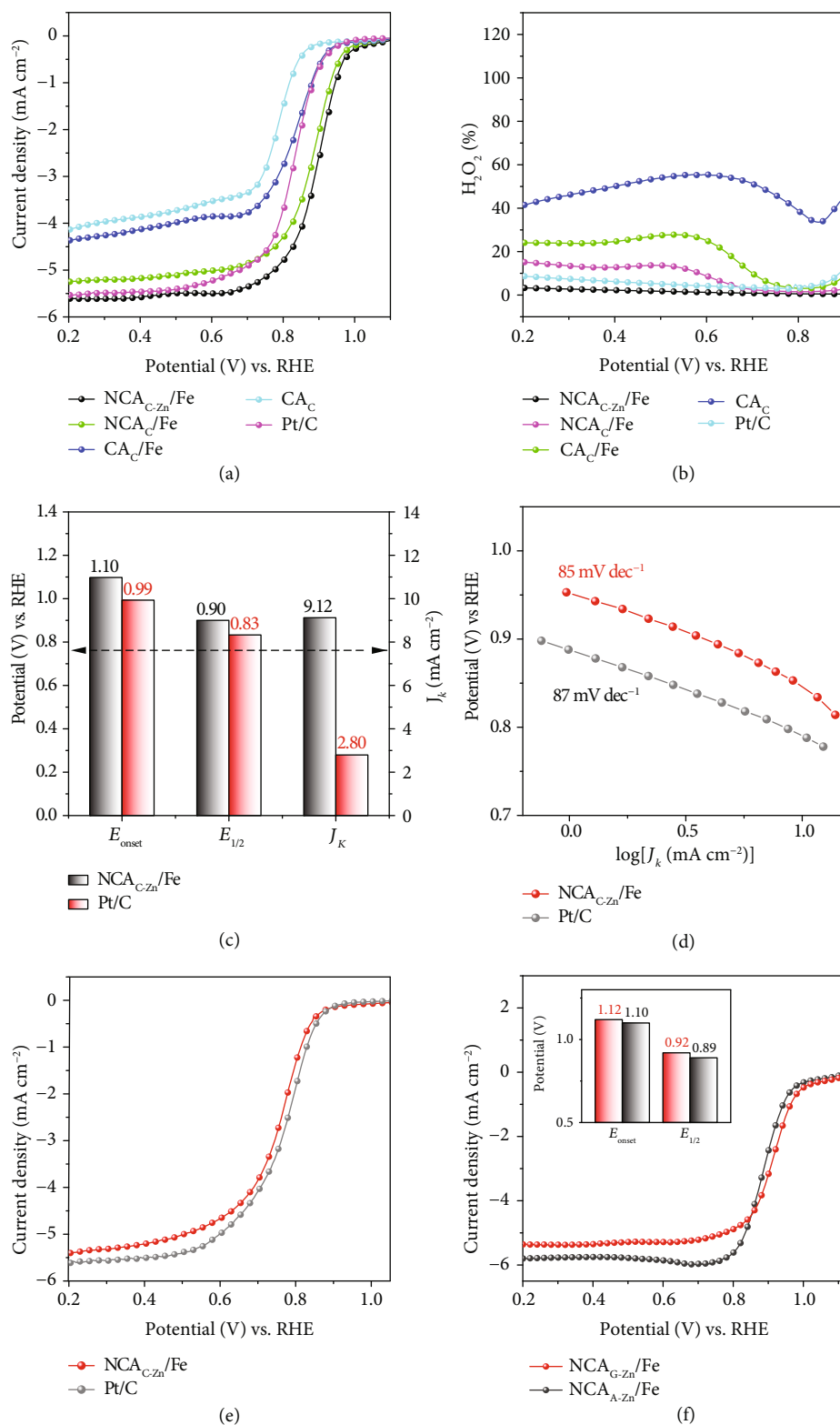


FIGURE 4: ORR performance. (a) ORR polarization curves of CA<sub>C</sub>, CA<sub>C</sub>/Fe, NCA<sub>C</sub>/Fe, and NCA<sub>C-Zn</sub>/Fe, as well as the Pt/C at 1600 rpm in 0.1 M KOH at the potential sweep rate of 5 mV s<sup>-1</sup>. (b) H<sub>2</sub>O<sub>2</sub> yield of CA<sub>C</sub>, CA<sub>C</sub>/Fe, NCA<sub>C</sub>/Fe, NCA<sub>C-Zn</sub>/Fe, and Pt/C. (c)  $E_{\text{onset}}$ ,  $E_{1/2}$ , and  $J_k$  (at +0.85 V) of the NCA<sub>C-Zn</sub>/Fe carbon aerogels and Pt/C catalyst. (d) Tafel plots of NCA<sub>C-Zn</sub>/Fe and Pt/C. (e) ORR performance in acidic media. ORR polarization curves of the NCA<sub>C-Zn</sub>/Fe and the Pt/C at 1600 rpm on RDE in 0.1 M HClO<sub>4</sub> at the potential sweep rate of 5 mV s<sup>-1</sup>. (f) ORR activity of aerogels derived from agar and gelatin hydrogels. ORR polarization curves of NCA<sub>A-Zn</sub>/Fe and NCA<sub>G-Zn</sub>/Fe as well as Pt/C at 1600 rpm on RDE in 0.1 M KOH at the potential sweep rate of 5 mV s<sup>-1</sup>.

$\text{dec}^{-1}$ ) in the high potential range, illustrating an efficient kinetic process of ORR on these two catalysts (Figure 4(d)). Besides, in contrast with Pt/C, the  $\text{NCA}_{\text{C-Zn}}/\text{Fe}$  exhibits remarkable durability and methanol tolerance (Figure S16). In addition, the  $E_{1/2}$  and diffusion-limited current density of  $\text{NCA}_{\text{C-Zn}}/\text{Fe}$  were comparable to those of Pt/C in acidic media (0.1 M  $\text{HClO}_4$ ), suggesting the high ORR activity of the single iron atom catalysts even at low pH (Figure 4(e)).

To distinguish the contributions of the Fe center and adjacent nonmetal atoms to the electrocatalytic activity, electrochemical measurements were then carried out with the addition of  $\text{SCN}^-$  as the poisoning species. One can see that upon the addition of 10 mM  $\text{SCN}^-$  into 0.1 M KOH, the  $E_{1/2}$  of  $\text{NCA}_{\text{C-Zn}}/\text{Fe}$  exhibited a negative shift of 20 mV (Figure S17). The relatively mild performance deterioration suggests that in addition to the Fe sites, adjacent nonmetal atoms also play a critical role in driving the catalytic reaction. This is actually in good agreement with the formation of  $\text{FeN}_x$  SW moieties in the carbon skeletons, where structural distortion leads to the activation of adjacent C atoms (Figures 3 and S12) [8].

Notably, other biomass hydrogels, such as gelatin and agar, can also be used as templates to fabricate nanowrinkled carbon aerogels embedded with single-metal atoms in a similar fashion. The resulting catalysts,  $\text{NCA}_{\text{G-Zn}}/\text{Fe}$  and  $\text{NCA}_{\text{A-Zn}}/\text{Fe}$ , both displayed excellent catalytic activities towards ORR in alkaline media, with an  $E_{1/2}$  of +0.92 and +0.89 V and an  $E_{\text{onset}}$  of +1.12 and 1.10 V, respectively (Figure 4(f) and inset). These results highlight the universality of the synthetic strategy in the preparation of high-performance ORR electrocatalysts (Figure S1).

**2.4. Electrocatalytic Activity towards OER and Zinc-Air Battery Performance.** The electrocatalytic activity of the  $\text{NCA}_{\text{C-Zn}}/\text{Fe}$  aerogels towards OER was then examined and compared with commercial  $\text{RuO}_2$  in 1 M KOH with iR correction. From Figure 5(a), one can see that for  $\text{NCA}_{\text{C-Zn}}/\text{Fe}$ , an overpotential ( $\eta_{10}$ ) of +370 mV was needed to achieve the current density of  $10 \text{ mA cm}^{-2}$ , a performance comparable to that of commercial  $\text{RuO}_2$  ( $\eta_{10} = +340 \text{ mV}$ ). The  $\text{NCA}_{\text{C-Zn}}/\text{Fe}$  also exhibits a Tafel slope of  $98 \text{ mV dec}^{-2}$ , close to that of  $\text{RuO}_2$  ( $71 \text{ mV dec}^{-2}$ ), signifying a favorable OER kinetic (Figure S18). Thanks to the excellent electrocatalytic performance towards both ORR and OER, the  $\text{NCA}_{\text{C-Zn}}/\text{Fe}$  SACs show a low potential difference ( $\Delta E$ ) of only 0.71 V between the OER potential at  $10 \text{ mA cm}^{-2}$  ( $E_{\text{OER},10}$ ) and the ORR potential at  $3 \text{ mA cm}^{-2}$  ( $E_{\text{ORR},3}$ ), much smaller than those of bifunctional M–N–C catalysts reported recently in the literature [11, 35, 36].

With such a remarkable bifunctional performance, the  $\text{NCA}_{\text{C-Zn}}/\text{Fe}$  aerogels were tested as the air-cathode for a Zn-air battery, in comparison with those using a commercial Pt/C- $\text{RuO}_2$  mixture (mass ratio 1 : 1), along with a Zn plate as the anode. From Figures 5(b) to 5(c), the  $\text{NCA}_{\text{C-Zn}}/\text{Fe}$ -Zn-air battery can be seen to show an open-circuit voltage (OCV) of 1.50 V and a maximum power density of  $231 \text{ mW cm}^{-2}$ , about 6 mV and  $20 \text{ mW cm}^{-2}$  higher than those of the Pt/C- $\text{RuO}_2$  counterpart. Figure 5(d) shows the correspond-

ing constant current discharge tests at various current densities (5, 10, 20, and  $50 \text{ mA cm}^{-2}$ ) of the two batteries. One can see that the  $\text{NCA}_{\text{C-Zn}}/\text{Fe}$ -Zn battery exhibited a much higher discharge voltage within a wide range of current densities (5 to  $50 \text{ mA cm}^{-2}$ ). At the constant current density of  $10 \text{ mA cm}^{-2}$ , the  $\text{NCA}_{\text{C-Zn}}/\text{Fe}$ -Zn battery displayed a stable and optimal potential of 1.36 V for 41 h. By normalizing the energy output to the weight of dissipated Zn, the calculated specific capacity and energy density were estimated to be  $780 \text{ mAh g}^{-1}$  and  $956 \text{ Wh kg}^{-1}$ , respectively, markedly higher than those of Pt/C- $\text{RuO}_2$  (Figure S19). Also, the small charge-discharge voltage gap of the  $\text{NCA}_{\text{C-Zn}}/\text{Fe}$ -Zn battery in Figure 5(e) indicates excellent rechargeability (Figure S20). Impressively, the battery also delivers a stable potential plateau in the charge-discharge test at the constant current density of  $10 \text{ mA cm}^{-2}$  during prolonged operation. After 1100 continuous charge-discharge cycles (400 s for each cycle), the  $\text{NCA}_{\text{C-Zn}}/\text{Fe}$ -Zn battery still afforded a high round-trip efficiency of 59% and a narrow discharge-recharge voltage gap of 0.79 V, much better than those of Pt/C- $\text{RuO}_2$  and other leading oxygen electrocatalysts reported in recent literature (Figure 5(f)) [5, 11, 37–40]. Taken together, these results demonstrate that the  $\text{NCA}_{\text{C-Zn}}/\text{Fe}$  aerogels derived from biomass hydrogels can be used as high-performance bifunctional oxygen electrodes for Zn-air batteries, thanks to its high open-circuit voltage, large power density, and superb durability.

### 3. Conclusion

In this study, a facile, scalable strategy was developed for the preparation of nanowrinkled carbon aerogels embedded with  $\text{FeN}_x$  active sites by utilizing biomass hydrogels as the precursors and reactors. The resulting nanowrinkled carbon aerogels ( $\text{NCA}_{\text{C-Zn}}/\text{Fe}$ ) showed an excellent and reversible ORR/OER electrocatalytic performance with a low voltage gap of only 0.71 V for oxygen electrocatalysis. With the obtained carbon aerogels as the (air) cathode catalysts of a Zn-air battery, the battery exhibited a higher open-circuit voltage, greater power density, and superior durability than that based on a mixture of commercial Pt/C- $\text{RuO}_2$  catalysts. First-principles calculation showed that  $\text{FeN}_x$  sites in Stone-Wales defect formed by the carbon nanowrinkles were most likely responsible for the excellent electrocatalytic activity. Results from the present study suggest that creating structural distortion of metal sites in carbon matrices can be exploited as an effective strategy for the design and engineering of advanced electrocatalysts based on atomically dispersed metal centers.

### 4. Materials and Methods

**4.1. Reagents.** Potassium hydroxide (KOH), iron(II) chloride tetrahydrate ( $\text{FeCl}_2 \cdot 4\text{H}_2\text{O}$ ),  $\text{SiO}_2$  nanoparticles (15 nm), zinc(II) acetate ( $\text{Zn}(\text{OAc})_2$ ), potassium thiocyanate (KSCN), gelatin, and agar were purchased from Aladdin Reagents (Shanghai, China). Perchloric acid ( $\text{HClO}_4$ ) and ammonium hydroxide ( $\text{NH}_4\text{OH}$ ) were purchased from Xiya Reagents (Chengdu, China). Chitosan and Nafion solution were



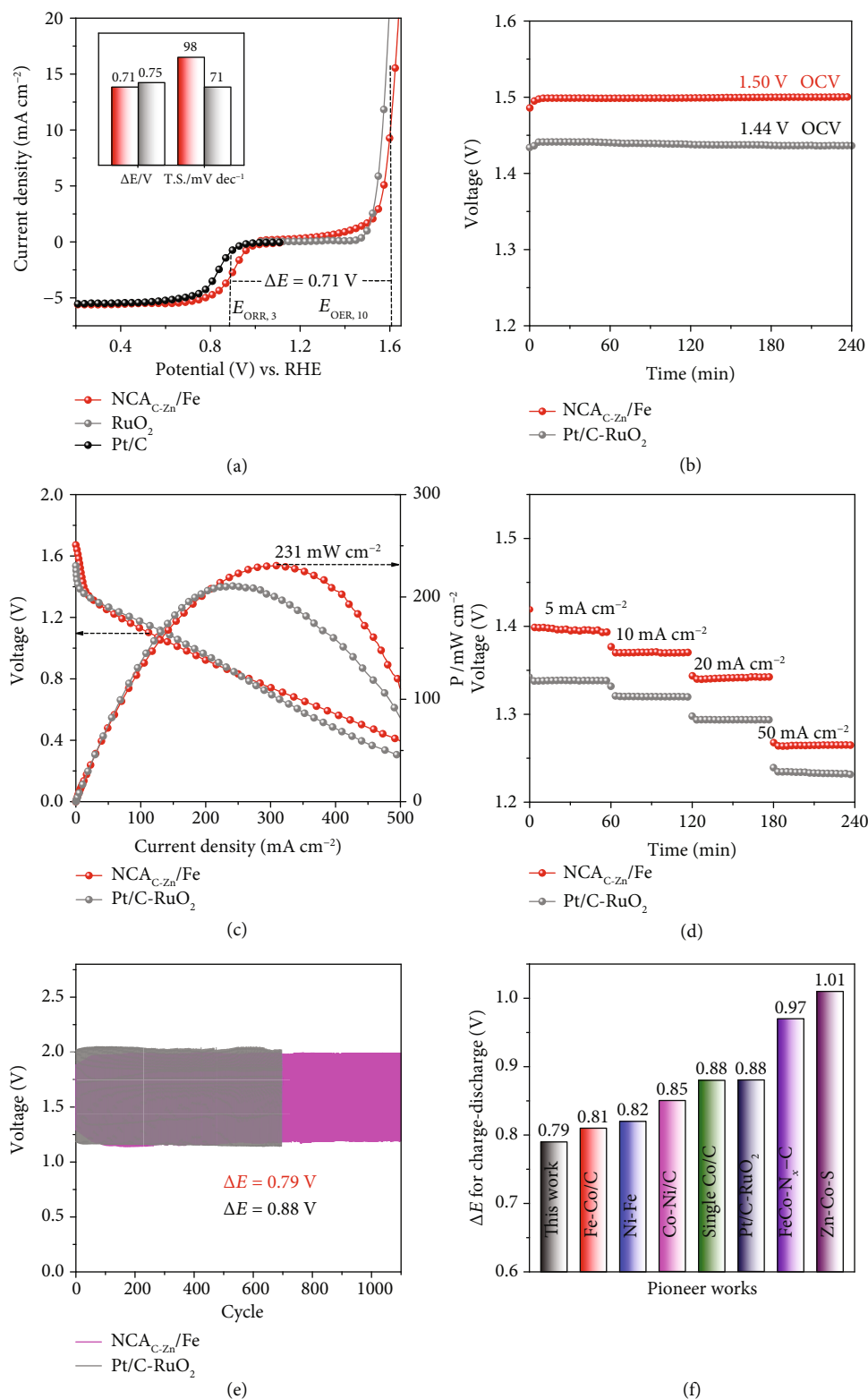


FIGURE 5: Zn-air performance tests. (a) Polarization curves for OER and ORR by NCA<sub>C-Zn</sub>/Fe and Pt/C-RuO<sub>2</sub>. Inset shows the corresponding ΔE between E<sub>j=3</sub> and E<sub>j=10</sub> and the Tafel slope of OER. (b) OCV and (c) power densities of Zn-air batteries assembled by NCA<sub>C-Zn</sub>/Fe and Pt/C-RuO<sub>2</sub>. (d) Discharge tests at various current densities (5, 10, 20, and 50 mA cm<sup>-2</sup>) of NCA<sub>C-Zn</sub>/Fe and Pt/C-RuO<sub>2</sub>. (e) Charge-discharge curves of Zn-air batteries assembled by NCA<sub>C-Zn</sub>/Fe and Pt/C-RuO<sub>2</sub> at 10 mA cm<sup>-2</sup> for 1100 cycles (400 s per cycle). (f) Comparison of charge-discharge voltage gap for NCA<sub>C-Zn</sub>/Fe with leading results reported in recent literature [5, 11, 37–40].

purchased from Sigma-Aldrich (USA). Commercial Pt/C (20 wt%) and high-purity zinc plate (99.999%) were obtained from Johnson Matthey. Polytetrafluoroethylene (PTFE, 60 wt%, D-210C) was purchased from Japan DaJin. All other reagents were analytical grade, and ultrapure water (Mill-Q, 18.3 M $\Omega$  cm) was used throughout this study.

**4.2. Instrumentation.** TEM studies were carried out with a T20 FEI Tecnai G2 instrument. Scanning electron microscopy images were obtained with a Hitachi S-4800 field-emission scanning electron microscope. STEM with EDS studies were performed on a JEOL JEM-ARM200CF with aberration-corrected STEM. Topography, maximum force, adhesion force, and current flow were measured using the Fast Force Mapping technique with an Oxford Instruments Asylum Cypher S AFM housed in an Ar-gas-filled glove box. Raman spectra were acquired with a Renishaw inVia Raman microscope. CD spectra were recorded on Jasco J-815 CD spectrometer (Japan). UV-vis spectra were acquired with a Shimadzu UV-2450 Spectrophotometer (Japan). ICP-OES studies were performed on a SPECTROBLUE SOP instrument. XRD and XPS measurements were carried out on a D/MAX2550 X-Ray Power Diffractometer and a Thermo Fisher-VG Scientific ESCALAB 250Xi X-Ray Photoelectron Spectrometer, respectively. N<sub>2</sub> adsorption-desorption isotherms were obtained with a Micromeritics ASAP 2020 Surface Area and Porosity Analyzer. Fe K-edge EXAFS measurements were performed at the Quick-EXAFS Beamline of the Taiwan Photon Source in transmission mode, and the results were analyzed by using the FeN<sub>x</sub>C<sub>y</sub> structural model with the Athena program. An RST 5200F electrochemical workstation (Zhengzhou, China) was used to perform the voltammetric measurements. Rotating Disk Electrode (RDE, Pine Research Instrument) tests were carried out at the rotation rates of 400 to 1600 rpm.

**4.3. Synthesis of Catalysts.** In a typical reaction, 60 mg of chitosan (CS), 40 mg of SiO<sub>2</sub> nanoparticles (15 nm), and 2.56 mL of acetic acid (1%) were placed in screw-cap vial under magnetic stirring for 90 min, into which was added 90  $\mu$ L of NH<sub>3</sub>H<sub>2</sub>O (20 wt%) to adjust the solution pH to 7.0. 200  $\mu$ L of 0.2 M Fe-phenanthroline (Fe(PM)<sub>3</sub><sup>2+</sup>) and 80  $\mu$ L of 1 M zinc acetate (Zn(OAc)<sub>2</sub>) were then added into the above solution under stirring. Sonication treatment for 6 min yielded a hydrogel, which was denoted as CS<sub>Si-Zn</sub>/FePM (“Si,” “Zn,” and “FePM” stand for SiO<sub>2</sub> nanoparticles, Zn<sup>2+</sup> ions, and Fe(PM)<sub>3</sub><sup>2+</sup>, respectively). The CS<sub>Si-Zn</sub>/FePM hydrogel obtained above was freeze-dried and then heated to 900°C at the heating rate of 5°C min<sup>-1</sup> in an Ar atmosphere (containing 3% H<sub>2</sub>). After heating at 900°C for 3 h, the sample was cooled down to room temperature and subjected to HF etching to remove SiO<sub>2</sub> nanoparticles, affording an Fe-N-codoped carbon aerogel, which was referred to as NCA<sub>C-Zn</sub>/Fe.

Three control samples were prepared in the same fashion except that only one or two of the starting materials (SiO<sub>2</sub> nanoparticles, Zn<sup>2+</sup> ions, and Fe(PM)<sub>3</sub><sup>2+</sup>) were used to prepare the biomass hydrogel precursors (i.e., CS<sub>Si</sub>, CS<sub>Si</sub>/Fe,

and CS<sub>Si</sub>/FePM). The corresponding aerogels were denoted as CA<sub>C</sub>, CA<sub>C</sub>/Fe, and NCA<sub>C</sub>/Fe, respectively.

**4.4. Electrochemistry.** Electrochemical tests were carried out in a three-electrode electrochemical cell with a graphite rod as the counter electrode and an Ag/AgCl (saturated KCl) electrode as the reference electrode. The Ag/AgCl reference electrode was calibrated against a reversible hydrogen electrode (RHE) and all potentials in the present study were referenced to this RHE. To prepare a catalyst ink, 3 mg of the catalysts obtained above was dispersed in a 475  $\mu$ L mixed solvent of H<sub>2</sub>O and ethanol ( $v:v=1:1$ ) and 25  $\mu$ L of a Nafion solution (5%) under sonication for 1 h to form a homogeneous dispersion (6 mg mL<sup>-1</sup>). For ORR tests, the catalyst ink was loaded onto a cleaned glassy carbon electrode at the catalyst loading of 250  $\mu$ g cm<sup>-2</sup> for cyclic voltammetry and 400  $\mu$ g cm<sup>-2</sup> for RDE and RRDE measurements in 0.1 M KOH, respectively. For OER tests, the catalyst was loaded onto a carbon paper at the mass loading of 1.0 mg cm<sup>-2</sup> in 1.0 M KOH.

In RDE measurements the disk current density ( $J$ ) is defined by the Koutecky-Levich (K-L) equation:

$$\frac{1}{J} = \frac{1}{J_L} + \frac{1}{J_K} = \frac{1}{B\omega^{1/2}} + \frac{1}{J_K}, \quad (1)$$

$$B = 0.2nFC_0(D_0)^{2/3}v^{-1/6},$$

where  $J_L$  is the limiting current density,  $J_K$  is the kinetic current density,  $\omega$  is the rotation rate,  $n$  is electron transfer number,  $F$  is the Faraday constant (96,485 C mol<sup>-1</sup>),  $C_0$  is the O<sub>2</sub> concentration in the electrolyte solution (1.2  $\times 10^{-6}$  mol cm<sup>-3</sup>), and  $v$  is the kinematic viscosity of the electrolyte (0.01 cm<sup>2</sup> s<sup>-1</sup> for 0.1 M KOH).  $J_K$  can be determined from the intercept of the K-L plot ( $J^{-1}$  vs.  $\omega^{-1/2}$ ).

In RRDE measurements, the H<sub>2</sub>O<sub>2</sub> yield and electron transfer number ( $n$ ) can be calculated by equation (2).

$$\%H_2O_2 = 200 \times \frac{I_r/N}{I_d + (I_r/N)}, \quad (2)$$

$$n = 4 \times \frac{I_d}{I_d + (I_r/N)},$$

where  $I_r$  and  $I_d$  are the ring current and disk current, respectively, and  $N$  is the collection efficiency of the ring electrode (0.37).

**4.5. Fabrication of Home-Made Zinc-Air Battery.** To make a zinc-air battery, a 6 M KOH solution containing 0.2 M zinc acetate was used as the electrolyte. A zinc plate was used as the anode. The air cathode was composed of three layers, i.e., a gas diffusion layer, a Ni foam layer, and a catalyst layer. The Ni foam was subject to sonication treatment in 0.1 M HCl, H<sub>2</sub>O, and ethanol consecutively, and vacuum dried at 80°C for 3 h. The catalyst layer was prepared by mixing 60 mg NCA<sub>C-Zn</sub>/Fe catalyst (or a mixture of 30 mg Pt/C and 30 mg RuO<sub>2</sub>), 10 mg acetylene black (as a conductive agent), and 30 mg PTFE emulsion. The total thickness of the cathode

was ca. 0.4 mm after compression with a manual tablet machine and vacuum dried at 80 °C for 3 h.

**4.6. DFT Calculations.** DFT calculations were carried out by Quantum ESPRESSO which is an open-source planewave code [41]. A two-dimensional supercell was built based on an 8 × 8 unit cell (127-129 atoms in total). For avoiding the interactions between periodic images, the vacuum at the z-axis was set at 14 Å. The ultrasoft pseudopotential was adopted [42]. The kinetic and charge density cutoff were set at 40 and 200 Ry, respectively. The 2 × 2 × 1 Monkhorst-Pack K-point grids were sampled for the supercell. The total energy was converged to 10<sup>-3</sup> eV for geometric relaxation. The Marzari-Vanderbilt smearing was adopted with a smearing of 0.01 Ry [43]. The electronic energy and force were converged to 10<sup>-8</sup> Ry and 10<sup>-4</sup> a.u., respectively. The phonon contribution to zero-point energy and entropy was calculated based on the density functional perturbation theory [44, 45]. STM calculations were carried out based on the Tersoff and Hamann approximation [46] as implemented in the open-source Quantum ESPRESSO package [41] at a bias of -1.0 or +1.0 V, as described in the literature [47].

## Conflicts of Interest

The authors declare no competing financial interests.

## Authors' Contributions

T. He synthesized the materials, conducted the electrochemical tests and morphological and structural characterization, and wrote the paper. B. Lu and Y. Ping carried out the DFT calculations. Y. Chen and Y. Wang provided important assistance in the synthesis of materials and linear sweep voltammetry measurements. Y. Zhang performed the high-angle annular dark-field scanning TEM and corresponding elemental mapping measurements. J. L. Davenport, A. P. Chen, A. Stram, A. Mordaunt, and J. Velasco, Jr. performed the AFM studies. C. Pao and M. Liu provided important assistance in data analysis of K-edge XANES and EXAFS. Z. Sun designed the experiments and revised the paper. Y. Zhang and S. Chen designed experiments, analyzed data, and finalized the paper (supervisors). Ting He and Bingzhang Lu contributed equally to this work.

## Acknowledgments

Y.Z. acknowledges support from the National Natural Science Foundation of China (21972169, 21773311, and 21473257) and Hunan Provincial Science and Technology Plan Project (2017TP1001). The authors thank Dr. Yongfeng Hu of the Canadian Light Source (Saskatoon) and Dr. Jeng-Lung Chen of the National Synchrotron Radiation Research Center (Taiwan) for their assistance in the acquisition of XANES and EXAFS data, and Dr. Yi Peng (UCSC) for helpful discussion. T.H. is supported by a research fellowship from the China Scholarship Council (201806370027). J.V.J. acknowledges support from the Army Research Office under

contract W911NF-17-1-0473. S.W.C. acknowledges support from the National Science Foundation (CHE-1710408 and CHE-1900235).

## Supplementary Materials

Table S1: BET surface area of CA<sub>C</sub>, CA<sub>C</sub>/Fe, NCA<sub>C</sub>/Fe, and NCA<sub>C-Zn</sub>/Fe. Table S2: EDS results of CA<sub>C</sub>, CA<sub>C</sub>/Fe, NCA<sub>C</sub>/Fe, and NCA<sub>C-Zn</sub>/Fe. Table S3: Fe contents in NCA<sub>C-Zn</sub>/Fe and NCA<sub>C</sub>/Fe determined by ICP-OES measurements. Table S4: elemental analysis by XPS measurements. Table S5: assignments of N species for different samples. Figure S1: schematic illustration of the preparation of NCA<sub>C-Zn</sub>/Fe carbon aerogels. Figure S2: SEM images of CS<sub>Si</sub>, CS<sub>Si</sub>/Fe, and CS<sub>Si</sub>/FePM. Figure S3: (a) CD and (b) UV-vis spectra of the series of biomass-derived hydrogels. Figure S4: TEM image of the NCA<sub>C-Zn</sub>/Fe aerogel. Figure S5: AFM images of NCA<sub>C-Zn</sub>/Fe aerogels: (a) topography image, (b) max force image, (c) adhesion force image, and (d) current flow image. Figure S6: (a) N<sub>2</sub> absorption-desorption isotherm and (b) pore size distribution of CA<sub>C</sub>, CA<sub>C</sub>/Fe, NCA<sub>C</sub>/Fe, and NCA<sub>C-Zn</sub>/Fe. Figure S7: XRD patterns of CA<sub>C</sub>, CA<sub>C</sub>/Fe, NCA<sub>C</sub>/Fe, and NCA<sub>C-Zn</sub>/Fe. Figure S8: EDS profiles of CA<sub>C</sub>, CA<sub>C</sub>/Fe, NCA<sub>C</sub>/Fe, and NCA<sub>C-Zn</sub>/Fe. The results are summarized in Table S2. Figure S9: (a) XPS of O 1s electrons of NCA<sub>C-Zn</sub>/Fe. XPS of the N 1s electrons of (b) NCA<sub>C</sub>/Fe and (c) CA<sub>C</sub>. Figure S10: EXAFS fitting curves for NCA<sub>C-Zn</sub>/Fe. Inset is the corresponding K-space profiles. Figure S11: top view of normal FeN<sub>3</sub> (a) and FeN<sub>3</sub> SW (b) moieties in graphene; side view of normal FeN<sub>3</sub> (c) and FeN<sub>3</sub> SW (d) moieties. Figure S12: simulated STM image (at a bias of 1.0 V) of (a) normal FeN<sub>4</sub> (a) and (b) Stone-Wales FeN<sub>4</sub>- (FeN<sub>4</sub> SW-) doped graphene sheets. Figure S13: EIS spectra of CA<sub>C</sub>, CA<sub>C</sub>/Fe, NCA<sub>C</sub>/Fe, and NCA<sub>C-Zn</sub>/Fe. Figure S14: RRDE polarization curves of CA<sub>C</sub>, CA<sub>C</sub>/Fe, NCA<sub>C</sub>/Fe, and NCA<sub>C-Zn</sub>/Fe, as well as Pt/C at 1600 rpm in 0.1 M KOH. Potential scan rate: 5 mV s<sup>-1</sup>. Figure S15: (a) electron transfer numbers of the biomass-derived carbon aerogels and Pt/C at different potentials; (b) average electron transfer numbers of CA<sub>C</sub> (4), CA<sub>C</sub>/Fe (3), NCA<sub>C</sub>/Fe (2), NCA<sub>C-Zn</sub>/Fe (1), and Pt/C. Figure S16: durability tests of NCA<sub>C-Zn</sub>/Fe and Pt/C; scan rate: 50 mV s<sup>-1</sup>; medium: O<sub>2</sub>-saturated 0.1 M KOH. (f) CV curves of the NCA<sub>C-Zn</sub>/Fe and commercial Pt/C as ORR catalysts in the presence or absence of 1 M MeOH. Figure S17: ORR polarization curves of NCA<sub>C-Zn</sub>/Fe in 0.1 M KOH with or without 10 mM KSCN. Figure S18: OER Tafel plots of (a) NCA<sub>C-Zn</sub>/Fe and (b) RuO<sub>2</sub>. Figure S19: specific capacity and energy density of NCA<sub>C-Zn</sub>/Fe and Pt/C-RuO<sub>2</sub>. Figure S20: charge-discharge tests of NCA<sub>C-Zn</sub>/Fe and Pt/C-RuO<sub>2</sub>. (*Supplementary Materials*)

## References

- [1] L. Ma, S. Chen, Z. Pei et al., "Single-site active iron-based bifunctional oxygen catalyst for a compressible and rechargeable zinc-air battery," *ACS Nano*, vol. 12, no. 2, pp. 1949-1958, 2018.

- [2] L. Zhu, D. Zheng, Z. Wang et al., "A confinement strategy for stabilizing ZIF-derived bifunctional catalysts as a benchmark cathode of flexible all-solid-state zinc-air batteries," *Advanced Materials*, vol. 30, no. 4, article 1805628, 2018.
- [3] Z.-Q. Liu, H. Cheng, N. Li, T. Y. Ma, and Y. Z. Su, "ZnCo<sub>2</sub>O<sub>4</sub> quantum dots anchored on nitrogen-doped carbon nanotubes as reversible oxygen reduction/evolution electrocatalysts," *Advanced Materials*, vol. 28, no. 19, pp. 3777–3784, 2016.
- [4] X.-T. Wang, T. Ouyang, L. Wang, J. H. Zhong, T. Ma, and Z. Q. Liu, "Redox-inert Fe<sup>3+</sup> Ions in octahedral sites of Co-Fe spinel oxides with enhanced oxygen catalytic activity for rechargeable zinc-air batteries," *Angewandte Chemie*, vol. 131, no. 38, pp. 13425–13430, 2019.
- [5] S. Li, C. Cheng, X. Zhao, J. Schmidt, and A. Thomas, "Active salt/silica-templated 2D mesoporous FeCo-N<sub>x</sub>-carbon as bifunctional oxygen electrodes for zinc-air batteries," *Angewandte Chemie, International Edition*, vol. 57, no. 7, pp. 1856–1862, 2018.
- [6] T. He, H. Xue, X. Wang et al., "Architecture of CoN<sub>x</sub> single clusters on nanocarbon as excellent oxygen reduction catalysts with high-efficient atomic utilization," *Nanoscale*, vol. 9, no. 24, pp. 8341–8348, 2017.
- [7] T. He, X. Wang, H. Wu et al., "In situ fabrication of defective CoN<sub>x</sub> single clusters on reduced graphene oxide sheets with excellent electrocatalytic activity for oxygen reduction," *ACS Applied Materials & Interfaces*, vol. 9, no. 27, pp. 22490–22501, 2017.
- [8] B. Lu, T. J. Smart, D. Qin et al., "Nitrogen and iron-codoped carbon hollow nanotubules as high-performance catalysts toward oxygen reduction reaction: a combined experimental and theoretical study," *Chemistry of Materials*, vol. 29, no. 13, pp. 5617–5628, 2017.
- [9] H. Cheng, M.-L. Li, C.-Y. Su, N. Li, and Z. Q. Liu, "Cu-Co bimetallic oxide quantum dot decorated nitrogen-doped carbon nanotubes: a high-efficiency bifunctional oxygen electrode for Zn-air batteries," *Advanced Functional Materials*, vol. 27, no. 30, article 1701833, 2017.
- [10] D. Li, Y. Jia, G. Chang et al., "A defect-driven metal-free electrocatalyst for oxygen reduction in acidic electrolyte," *Chem*, vol. 4, no. 10, pp. 2345–2356, 2018.
- [11] W. Zang, A. Sumboja, Y. Ma et al., "Single Co atoms anchored in porous N-doped carbon for efficient zinc-air battery cathodes," *ACS Catalysis*, vol. 8, no. 10, pp. 8961–8969, 2018.
- [12] Y. Peng, B. Lu, and S. Chen, "Carbon-supported single atom catalysts for electrochemical energy conversion and storage," *Advanced Materials*, vol. 30, no. 48, article e1801995, 2018.
- [13] H. Xue, T. He, J. M. Chabu et al., "Iron single clusters anchored on N-doped porous carbon as superior trace-metal catalysts toward oxygen reduction," *Advanced Materials Interfaces*, vol. 5, no. 7, article 1701345, 2018.
- [14] Y. Peng, B. Lu, L. Chen et al., "Hydrogen evolution reaction catalyzed by ruthenium ion-complexed graphitic carbon nitride nanosheets," *Journal of Materials Chemistry A*, vol. 5, no. 34, pp. 18261–18269, 2017.
- [15] Y. Deng, B. Chi, J. Li et al., "Atomic Fe-doped MOF-derived carbon polyhedrons with high active-center density and ultra-high performance toward PEM fuel cells," *Advanced Energy Materials*, vol. 9, no. 13, article 1802856, 2019.
- [16] Q. Deng, J. Zhao, T. Wu, G. Chen, H. A. Hansen, and T. Vegge, "2D transition metal-TCNQ sheets as bifunctional single-atom catalysts for oxygen reduction and evolution reaction (ORR/OER)," *Journal of Catalysis*, vol. 370, pp. 378–384, 2019.
- [17] X. Wang, Z. Chen, X. Zhao et al., "Regulation of coordination number over single Co Sites: Triggering the efficient electroreduction of CO<sub>2</sub>," *Angewandte Chemie*, vol. 130, no. 7, pp. 1962–1966, 2018.
- [18] Y. Deng, B. Chi, X. Tian et al., "g-C<sub>3</sub>N<sub>4</sub> promoted MOF derived hollow carbon nanopolyhedra doped with high density/fraction of single Fe atoms as an ultra-high performance non-precious catalyst towards acidic ORR and PEM fuel cells," *Journal of Materials Chemistry A*, vol. 7, no. 9, pp. 5020–5030, 2019.
- [19] V. Budarin, J. H. Clark, J. J. E. Hardy et al., "Starbons: new starch-derived mesoporous carbonaceous materials with tunable properties," *Angewandte Chemie*, vol. 118, no. 23, pp. 3866–3870, 2006.
- [20] S. De, A. M. Balu, J. C. van der Waal, and R. Luque, "Biomass-derived porous carbon materials: synthesis and catalytic applications," *ChemCatChem*, vol. 7, no. 11, pp. 1608–1629, 2015.
- [21] N. Sahiner, "Soft and flexible hydrogel templates of different sizes and various functionalities for metal nanoparticle preparation and their use in catalysis," *Progress in Polymer Science*, vol. 38, no. 9, pp. 1329–1356, 2013.
- [22] C. Lv, W. Xu, H. Liu et al., "3D sulfur and nitrogen codoped carbon nanofiber aerogels with optimized electronic structure and enlarged interlayer spacing boost potassium-ion storage," *Small*, vol. 15, no. 23, article 1900816, 2019.
- [23] H. Li, X. Zhao, H. Liu et al., "Sub-1.5 nm ultrathin CoP nanosheet aerogel: efficient electrocatalyst for hydrogen evolution reaction at all pH values," *Small*, vol. 14, no. 41, article 1802824, 2018.
- [24] Z. Sun, F. Lv, L. Cao, L. Liu, Y. Zhang, and Z. Lu, "Multistimuli-responsive moldable supramolecular hydrogels cross-linked by ultrafast complexation of metal ions and biopolymers," *Angewandte Chemie International Edition*, vol. 54, no. 27, pp. 7944–7948, 2015.
- [25] B. Biswas, A. Al-Hunaiti, M. T. Räisänen et al., "Efficient and selective oxidation of primary and secondary alcohols using an iron(III)/phenanthroline complex: structural studies and catalytic activity," *European Journal of Inorganic Chemistry*, vol. 2012, no. 28, pp. 4479–4485, 2012.
- [26] X. Sun, G.-P. Hao, X. Lu et al., "High-defect hydrophilic carbon cuboids anchored with Co/CoO nanoparticles as highly efficient and ultra-stable lithium-ion battery anodes," *Journal of Materials Chemistry A*, vol. 4, no. 26, pp. 10166–10173, 2016.
- [27] G.-P. Hao, G. Mondin, Z. Zheng et al., "Unusual ultra-hydrophilic porous carbon cuboids for atmospheric-water capture," *Angewandte Chemie International Edition*, vol. 54, no. 6, pp. 1941–1945, 2015.
- [28] S. H. Cho and S.-M. Park, "Electrochemistry of conductive Polymers 39. Contacts between conducting polymers and noble metal nanoparticles studied by current-sensing atomic force microscopy," *The Journal of Physical Chemistry B*, vol. 110, no. 51, pp. 25656–25664, 2006.
- [29] H. J. Lee and S.-M. Park, "Electrochemistry of conductive polymers. 30. Nanoscale measurements of doping distributions and current-voltage characteristics of electrochemically deposited polypyrrole films," *The Journal of Physical Chemistry B*, vol. 108, no. 5, pp. 1590–1595, 2004.

- [30] C. Zhu, Q. Shi, B. Z. Xu et al., “Hierarchically Porous M-N-C (M = Co and Fe) Single-Atom Electrocatalysts with Robust  $MN_x$  Active Moieties Enable Enhanced ORR Performance,” *Advanced Energy Materials*, vol. 8, no. 29, article 1801956, 2018.
- [31] Y. Yang, Z. Lun, G. Xia, F. Zheng, M. He, and Q. Chen, “Non-precious alloy encapsulated in nitrogen-doped graphene layers derived from MOFs as an active and durable hydrogen evolution reaction catalyst,” *Energy & Environmental Science*, vol. 8, no. 12, pp. 3563–3571, 2015.
- [32] G. Wan, P. Yu, H. Chen et al., “Engineering single-atom cobalt catalysts toward improved electrocatalysis,” *Small*, vol. 14, no. 15, article 1704319, 2018.
- [33] R. Jiang, L. Li, T. Sheng, G. Hu, Y. Chen, and L. Wang, “Edge-site engineering of atomically dispersed Fe-N<sub>4</sub> by selective C-N bond cleavage for enhanced oxygen reduction reaction activities,” *Journal of the American Chemical Society*, vol. 140, no. 37, pp. 11594–11598, 2018.
- [34] W. Xia, A. Mahmood, Z. Liang, R. Zou, and S. Guo, “Earth-abundant nanomaterials for oxygen reduction,” *Angewandte Chemie International Edition*, vol. 55, no. 8, pp. 2650–2676, 2016.
- [35] H. Jiang, Y. Liu, W. Li, and J. Li, “Co nanoparticles confined in 3D nitrogen-doped porous carbon foams as bifunctional electrocatalysts for long-life rechargeable Zn-air batteries,” *Small*, vol. 14, no. 13, 2018.
- [36] S. Liu, M. Wang, X. Sun et al., “Facilitated oxygen chemisorption in heteroatom-doped carbon for improved oxygen reaction activity in all-solid-state zinc-air batteries,” *Advanced Materials*, vol. 30, no. 4, article 1704898, 2018.
- [37] X. Wu, X. Han, X. Ma et al., “Morphology-controllable synthesis of Zn-Co-mixed sulfide nanostructures on carbon fiber paper toward efficient rechargeable zinc-air batteries and water electrolysis,” *ACS Applied Materials & Interfaces*, vol. 9, no. 14, pp. 12574–12583, 2017.
- [38] W. Niu, S. Pakhira, K. Marcus, Z. Li, J. L. Mendoza-Cortes, and Y. Yang, “Apically dominant mechanism for improving catalytic activities of N-doped carbon nanotube arrays in rechargeable zinc-air battery,” *Advanced Energy Materials*, vol. 8, no. 20, article 1800480, 2018.
- [39] K. Fu, Y. Wang, L. Mao et al., “Rational assembly of hybrid carbon nanotubes grafted on the carbon nanofibers as reliable and robust bifunctional catalyst for rechargeable zinc-air battery,” *Journal of Power Sources*, vol. 421, pp. 68–75, 2019.
- [40] Y. Fan, S. Ida, A. Staykov et al., “Ni-Fe nitride nanoplates on nitrogen-doped graphene as a synergistic catalyst for reversible oxygen evolution reaction and rechargeable Zn-air battery,” *Small*, vol. 13, no. 25, article 1700099, 2017.
- [41] P. Giannozzi, S. Baroni, N. Bonini et al., “QUANTUM ESPRESSO: a modular and open-source software project for quantum simulations of materials,” *Journal of Physics: Condensed Matter*, vol. 21, no. 39, article 395502, 2009.
- [42] K. F. Garrity, J. W. Bennett, K. M. Rabe, and D. Vanderbilt, “Pseudopotentials for high-throughput DFT calculations,” *Computational Materials Science*, vol. 81, pp. 446–452, 2014.
- [43] N. Marzari, D. Vanderbilt, A. De Vita, and M. C. Payne, “Thermal contraction and disordering of the Al(110) surface,” *Physical Review Letters*, vol. 82, no. 16, pp. 3296–3299, 1999.
- [44] S. Baroni, S. de Gironcoli, A. Dal Corso, and P. Giannozzi, “Phonons and related crystal properties from density-functional perturbation theory,” *Reviews of Modern Physics*, vol. 73, no. 2, pp. 515–562, 2001.
- [45] Y. Li and G. Galli, “Electronic and spectroscopic properties of the hydrogen-terminated Si(111) surface from *ab initio* calculations,” *Physical Review B*, vol. 82, no. 4, article 045321, 2010.
- [46] J. Tersoff and D. R. Hamann, “Theory and application for the scanning tunneling microscope,” *Physical Review Letters*, vol. 50, no. 25, pp. 1998–2001, 1983.
- [47] S.-O. Guillaume, B. Zheng, J.-C. Charlier, and L. Henrard, “Electronic properties and STM images of doped bilayer graphene,” *Physical Review B*, vol. 85, no. 3, article 035444, 2012.